



# Electrochemical catalytic mechanism of N-doped graphene for enhanced H<sub>2</sub>O<sub>2</sub> yield and in-situ degradation of organic pollutant

Pei Su<sup>a,b,c,d</sup>, Minghua Zhou<sup>a,b,c,d,\*</sup>, Xiaoye Lu<sup>a,b,c,d</sup>, Weilu Yang<sup>a,b,c,d</sup>,  
Gengbo Ren<sup>a,b,c,d</sup>, Jingju Cai<sup>a,b,c,d</sup>

<sup>a</sup> Key Laboratory of Pollution Process and Environmental Criteria, Ministry of Education, College of Environmental Science and Engineering, Nankai University, Tianjin, 300350, China

<sup>b</sup> Tianjin Key Laboratory of Urban Ecology Environmental Remediation and Pollution Control, College of Environmental Science and Engineering, Nankai University, Tianjin, 300350, China

<sup>c</sup> Tianjin Advanced Water Treatment Technology International Joint Research Center, College of Environmental Science and Engineering, Nankai University, Tianjin, 300350, China

<sup>d</sup> Tianjin Key Laboratory of Environmental Technology for Complex Trans-Media Pollution, Nankai University, Tianjin, 300350, China

## ARTICLE INFO

### Keywords:

N-doped graphene  
In-situ catalytic mechanism  
Electro-Fenton  
Oxygen reduction reaction  
Organic pollutant degradation

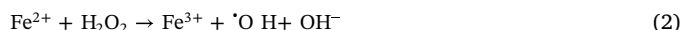
## ABSTRACT

Highly efficient electrochemical advanced oxidation processes (EAOPs) based on carbon catalysts are promising and green technologies for environmental remediation. Herein, for the purpose of cost-effectiveness, wide pH suitability and excellent reusability, graphite felt modified with regulatable N-doped graphene was developed as a cathode to electrochemically generate H<sub>2</sub>O<sub>2</sub> with high yield and selectivity, and efficiently catalyze H<sub>2</sub>O<sub>2</sub> to form <sup>•</sup>OH for organic pollutants degradation by in-situ metal-free EAOPs. Particularly, the catalytic mechanism of N-doped graphene for enhanced performance was explored. Optimized N-doped graphene showed a very high H<sub>2</sub>O<sub>2</sub> generation rate of 8.6 mg/h/cm<sup>2</sup>, low electric energy consumption (9.8 kW h/kg) and high H<sub>2</sub>O<sub>2</sub> selectivity of 78.02% in neutral pH solution. Compared with electro-Fenton (EF), this in-situ metal-free EAOPs on N-doped graphene displayed significant improvement on the degradation performance of organic pollutants in neutral and alkaline solutions, and was certified to be less affected by initial pH. The pyridinic N and C=C in N-doped graphene enhanced the onset potential while graphite N determined the disk current of oxygen reduction reaction (ORR) process. Most importantly, it proved that the introduction of graphite N could promote the 2e<sup>-</sup> ORR process for H<sub>2</sub>O<sub>2</sub> generation, and the presence of pyridinic N could catalyze H<sub>2</sub>O<sub>2</sub> to the production of <sup>•</sup>OH. Taken phenol as target pollutant, <sup>•</sup>OH generated by N-doped graphene accounted for 80.72% while O<sub>2</sub><sup>•-</sup> contributed 19.28% to its degradation, based on which a possible mechanism for phenol degradation was proposed. Moreover, in-situ metal-free EAOPs showed excellent stability, reusability and performance for various organic pollutants degradation. This work would shed light on the catalytic mechanism for metal-free EAOPs, and thus promote its application for organic pollutants degradation.

## 1. Introduction

Recently electrochemical advanced oxidation processes (EAOPs) based on non-selective oxidation of organic pollutants by <sup>•</sup>OH [1,2], have attracted great attention in the field of wastewater treatment due to their advantages of high mineralization efficiency for organic pollutants, no secondary pollution, and wide range of applications [3–5]. Especially, electro-Fenton (EF) has broad application prospects, in which H<sub>2</sub>O<sub>2</sub> is generated in-situ by oxygen reduction reaction (ORR) (Eq. (1)) and powerful <sup>•</sup>OH (Eq. (2)) could be formed in the presence of

catalyst (e.g., iron ion, or iron oxides) [6].



However, EF is still limited by intrinsic drawbacks of narrow pH range (pH ~ 3 is optimal) and the iron sludge production since Fe<sup>2+</sup> is easy to form flocculation in alkaline conditions [6–8].

It is well acknowledged that cathode material plays an important role in H<sub>2</sub>O<sub>2</sub> yield and EF performance. In the past decades, many noble metals and metal alloys have been suggested as prospective electro-

\* Corresponding author at: Key Laboratory of Pollution Process and Environmental Criteria, Ministry of Education, College of Environmental Science and Engineering, Nankai University, Tianjin, 300350, China.

E-mail address: [zhoumh@nankai.edu.cn](mailto:zhoumh@nankai.edu.cn) (M. Zhou).

<https://doi.org/10.1016/j.apcatb.2018.12.075>

Received 15 September 2018; Received in revised form 21 December 2018; Accepted 31 December 2018

Available online 02 January 2019

0926-3373/© 2019 Elsevier B.V. All rights reserved.

catalysts, however, carbon-based materials are supposed to be interesting alternatives to precious metals, including carbon black [9–11], carbon nanotubes [12–14], activated carbon [15,16], graphene [17–20], carbon fiber [17,21], and carbon felt [10,11,22]. Among them, graphene, two-dimensional (2D) material of  $sp^2$  hybrid carbon atoms, has been recently used as an effective catalyst for  $H_2O_2$  production due to its high specific surface area, outstanding electrical conductivity, and low resistivity [18,23–25]. Moreover, many chemical or electrochemical modification methods have been proposed to improve the yield of  $H_2O_2$ , and graphite felt modified with carbon black has also been proved to be cost-effective to achieve high  $H_2O_2$  yields [7,10,11,20].

On the other hand, ORR on the cathode determines the  $H_2O_2$  selectivity, which mainly consists of  $2e^-$  process (Eq. (1)) that generating  $H_2O_2$  and  $4e^-$  process that generating  $H_2O$  (Eq. (3)).



At present, heteroatoms (e.g., N, S, B) doped carbon materials have attracted great interests because it would be conducive to the adsorption of  $O_2$  to enhance ORR activity and electrochemical activity [26–30]. Most of heteroatoms doped carbon materials mainly occurred  $4e^-$  process to produced  $H_2O$  of ORR for energy conversion, but the introduction of the N element into carbon materials is different from the other elements. N-doped carbon materials could realize  $H_2O_2$  production in process of electron transfer [31,32]. Moreover, electrochemical generation of  $H_2O_2$  via  $2e^-$  process was supposed to be a facile, cost-effective and ecofriendly way enabling local, on-demand production [33–35]. Particularly, some recent works demonstrated that nitrogen-doped carbon materials could increase moderate activity for  $H_2O_2$  synthesis [36–43]. Furthermore, our findings proved that nitrogen-doped graphene could also act as catalyst to convert generated  $H_2O_2$  into free radicals [44]. Therefore, a novel in-situ metal-free EAOPs was developed for promising degradation of organic pollutants, solving the two major shortcomings of EF. However, there is still very limited understanding in the active sites on this electro-catalyst and how to efficiently promote the conversion of the electrochemically generated  $H_2O_2$  into powerful  $\cdot OH$ , which would be essential but still a big challenge since the catalytic mechanism regulating the activity and selectivity on active sites are still unclear.

Herein, N-doped graphene ( $N_x$ -GE) (x: the mass ratio of melamine to graphene) was synthesized by annealed of melamine and graphene, through which different N-doped contents could be regulated since these surface nitrogen-containing functional groups were postulated to be the active sites [45,46]. The effects of ratio of melamine/graphene in precursors on the electrochemical generation of  $H_2O_2$  and degradation performance of organic pollutants were investigated taking phenol as target pollutant. Our works confirmed that the cathode exhibited higher activity, selectivity and stability after N doped on graphene. Furthermore, the free radical species were detected and their contributions for phenol removal were quantified, and ability of  $H_2O_2$  to catalyze  $\cdot OH$  was analyzed by electrochemical characterizations. The differences in the phenol removal by in-situ metal-free EAOPs and EF were also compared, overcoming intrinsic drawbacks of narrow pH range and the iron sludge production in EF. More importantly, the effect of different nitrogen species on ORR activity and production and catalysis of  $H_2O_2$  were discussed. It proved that the introduction of graphite N could promote the  $2e^-$  ORR process for  $H_2O_2$  generation, and the presence of pyridinic N could catalyze  $H_2O_2$  to the production of  $\cdot OH$ . These findings would shed light on the catalytic mechanism for metal-free EAOPs, and thus promote its application for organic pollutants degradation.

## 2. Materials and methods

### 2.1. N-GE synthesis and graphite felt modification

Melamine was selected as nitrogen source for N-GE. First, the

graphene prepared by electrochemical exfoliation of graphite foil [24] was dissolved in ethanol, and melamine with different ratio to graphene (1:1–5) was added. Then, an appropriate amount of formaldehyde solution (37% wt.) was added. After the solvent was evaporated at  $80^\circ C$ , the dried mixed powder was annealed at  $950^\circ C$  ( $10^\circ C/min$ ) under nitrogen atmosphere for 5 h to obtain  $N_x$ -GE. The obtained  $N_x$ -GE and carbon black (CB) were mixed with ethanol, deionized water and polytetrafluorethylene (PTFE), and then the mixture paste was coated on graphite felt ( $4\text{ cm} \times 2.5\text{ cm}$ ). After drying in air, the modified graphite felt was annealed at  $360^\circ C$  under nitrogen atmosphere for 30 min to obtain  $N_x$ -GE-graphite felt ( $N_x$ -GE(CB)-GF, after referred to as  $N_x$ -GE-GF).

### 2.2. Physical characterization and EIS measurement

The microscopic morphology of  $N_x$ -GE was characterized by scanning electron microscopy (SEM) (LEO-1530VP, Germany), and transmission electron microscopy (TEM) (JEM-2800, Japan). Raman spectra were measured with a Renishaw Modular Raman spectrometer equipped with a Stellar Pro Argon-ion laser at 514 nm (50 mW). X-ray photoelectron spectroscopy (XPS) (Thermo Scientific ESCALAB 250Xi) was characterized with Mono Al K $\alpha$  radiation to analyze the surface chemical element compositions. Fourier Transform infrared spectroscopy (FTIR) spectra were obtained using TENSOR 37 spectrometer. The contact angle of water on the material surface was examined by a contact angle meter (JC2000X, China) with a water drop volume of 10  $\mu L$ .

Electrochemical impedance spectroscopy (EIS) was carried with the CHI 760E potentiostat (CH Instruments, Chenhua, Shanghai, China) in a three-electrode system using modified graphite felt, platinum sheet and saturated calomel electrode (SCE) as the working electrode, counter electrode, and reference electrode, respectively. EIS was measured at the open circuit potential in a frequency of 0.01 Hz–100 kHz with the amplitude of 10 mV to get the ohmic resistance ( $R_o$ ), diffusion resistance ( $R_d$ ), and charge transfer resistance ( $R_{ct}$ ).

### 2.3. Rotating disk electrode (RDE) and rotating ring disk electrode (RRDE) measurements

To test the oxygen reduction activity of  $N_x$ -GE, RDE and RRDE (Pine Instruments, USA) were accomplished with the CHI 760E potentiostat in a three-electrode system. The working electrode, counter electrode, and reference electrode were a glassy carbon electrode, platinum sheets, and Ag/AgCl electrode, respectively. The catalyst ink was prepared by blending 5 mg catalyst powder with 600  $\mu L$  water, 300  $\mu L$  ethanol and 100  $\mu L$  Nafion solutions (0.5 wt. %) in an ultrasonic bath for 30 min. The 10  $\mu L$  of the resulting catalyst ink was drop-casted onto the glassy carbon (GC) electrode. The final electrode catalyst loading was 0.25 mg/cm $^2$ .

Cyclic voltammetry (CV) was measured by RDE in  $N_2$  and  $O_2$ -saturated 50 mM  $Na_2SO_4$  aqueous solution respectively, with the potential interval of  $-0.8\text{ V}$  to  $0\text{ V}$  at a scan rate of 100 mV/s. Linear sweep voltammetry (LSV) by RDE was measured at different rotation speed between 425 and 2500 rpm with a scan rate of 10 mV/s. Activity of graphene per unit mass (mass activity) was calculated from the LSV result to illustrate the amount of active sites of  $N_x$ -GE. RRDE was measured from  $-1.1\text{ V}$  to  $0.1\text{ V}$  at 10 mV/s with the ring potential at 1.0 V at different rotation speeds. As shown in the schematic diagram of kinetics in ORR process in the supporting information, the ORR processes mainly included  $2e^-$   $H_2O_2$  production process ( $k_1$ ) and  $4e^-$   $H_2O$  production process ( $k_1'$ ).  $H_2O_2$  continued to obtain  $2e^-$  to generate  $H_2O$  ( $k_2$ ), and  $H_2O_2$  catalyzed to produce  $\cdot OH$  ( $k_3$ ) process (Fig. S1) [47–49]. The related rate constants ( $k_1'$ ,  $k_1$  and  $k_2$ ) for kinetics were calculated with the formulas (1), (2) and (3) in supporting information [49,50]. The electron transfer number ( $n$ ) and hydrogen peroxide selectivity (%) ( $H_2O_2$ ) were calculated by the following formulas [49]:

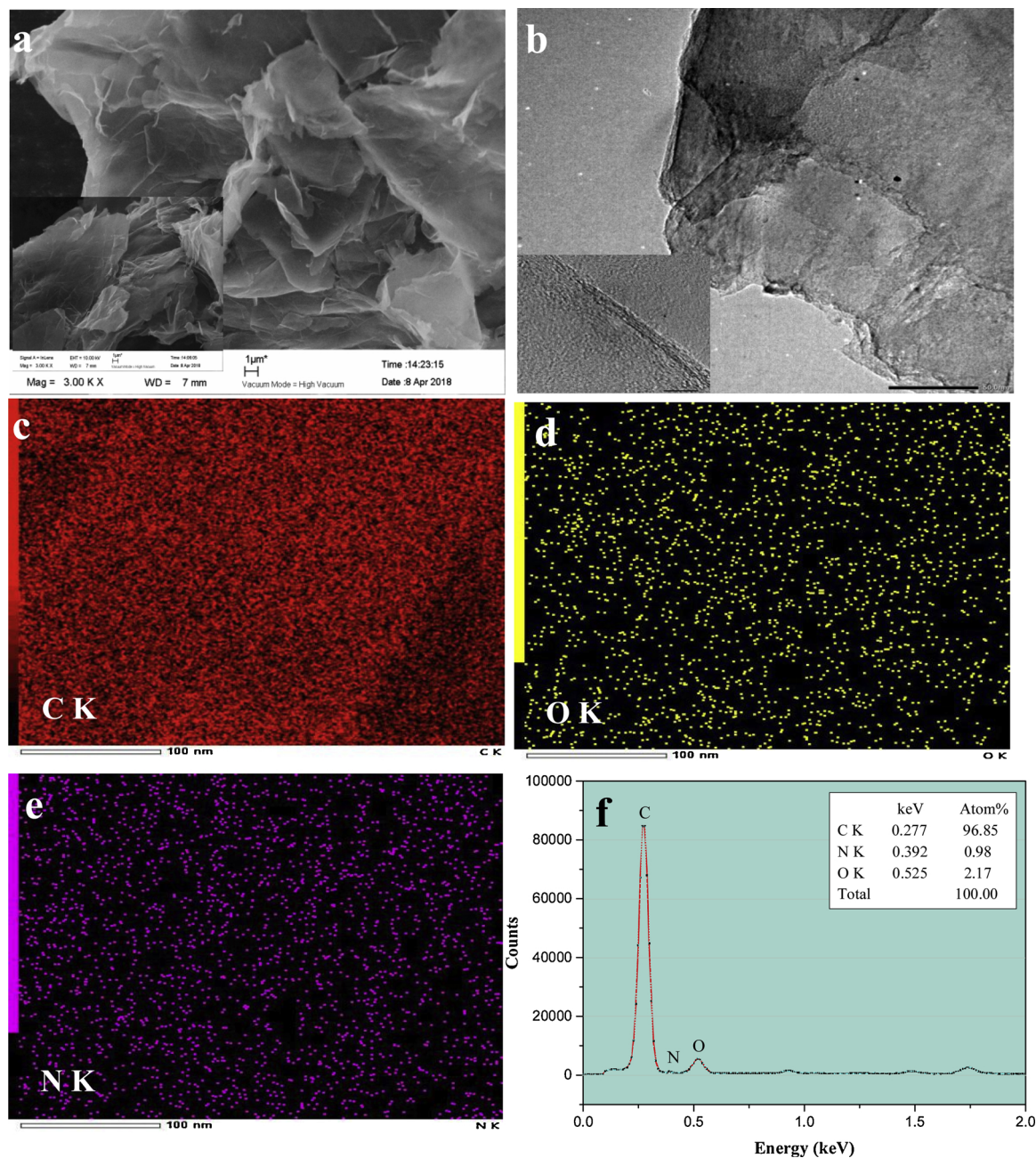


Fig. 1. SEM image (a) and TEM image (b) of N-GE; mapping of the C, O, N elements of N-GE (c–d); EDX pattern of N-GE (f).

$$n = \frac{4 \times I_d}{I_d + \frac{I_r}{N}} \quad (4)$$

$$\%H_2O_2 = \frac{2 \times \frac{I_r}{N}}{I_d + \frac{I_r}{N}} \times 100\% \quad (5)$$

Where  $I_d$  is the disk current (mA),  $I_r$  is the ring current (mA) and  $N$  is the collection efficient (0.383).

#### 2.4. Generation of $H_2O_2$ and $\cdot OH$ with in-situ metal-free EAOPs

Experiments were tested in 100 ml reactor containing 50 mM  $Na_2SO_4$  solution. The anode and cathode were DSA ( $2 \times 4 \text{ cm}^2$ ) and a modified graphite felt (effective area was  $5 \text{ cm}^2$ ), respectively. Potassium oxalate-spectrophotometric method was used to determine  $H_2O_2$  concentration and the current efficiency (CE) could be calculated

as follows [51]:

$$CE = \frac{nFCV}{\int_0^t Idt} \times 100\% \quad (6)$$

Where  $n$  is the number of electrons transferred,  $F$  is the Faraday constant (96,485 C/mol),  $C$  is the concentration of  $H_2O_2$  (mg/L),  $V$  is the bulk volume (L),  $I$  is the current (A) and  $t$  is the time (s).

Electric energy consumption (EEC) could be calculated by the following formula [51]:

$$EEC = \frac{1000UIt}{CV_s} \quad (7)$$

Where  $U$  is the voltage (V),  $I$  is the current (A),  $t$  is the time (h),  $V_s$  is the bulk volume (L), and  $C$  is the concentration of  $H_2O_2$  (mg/L) or concentration of phenol removal (mg/L).



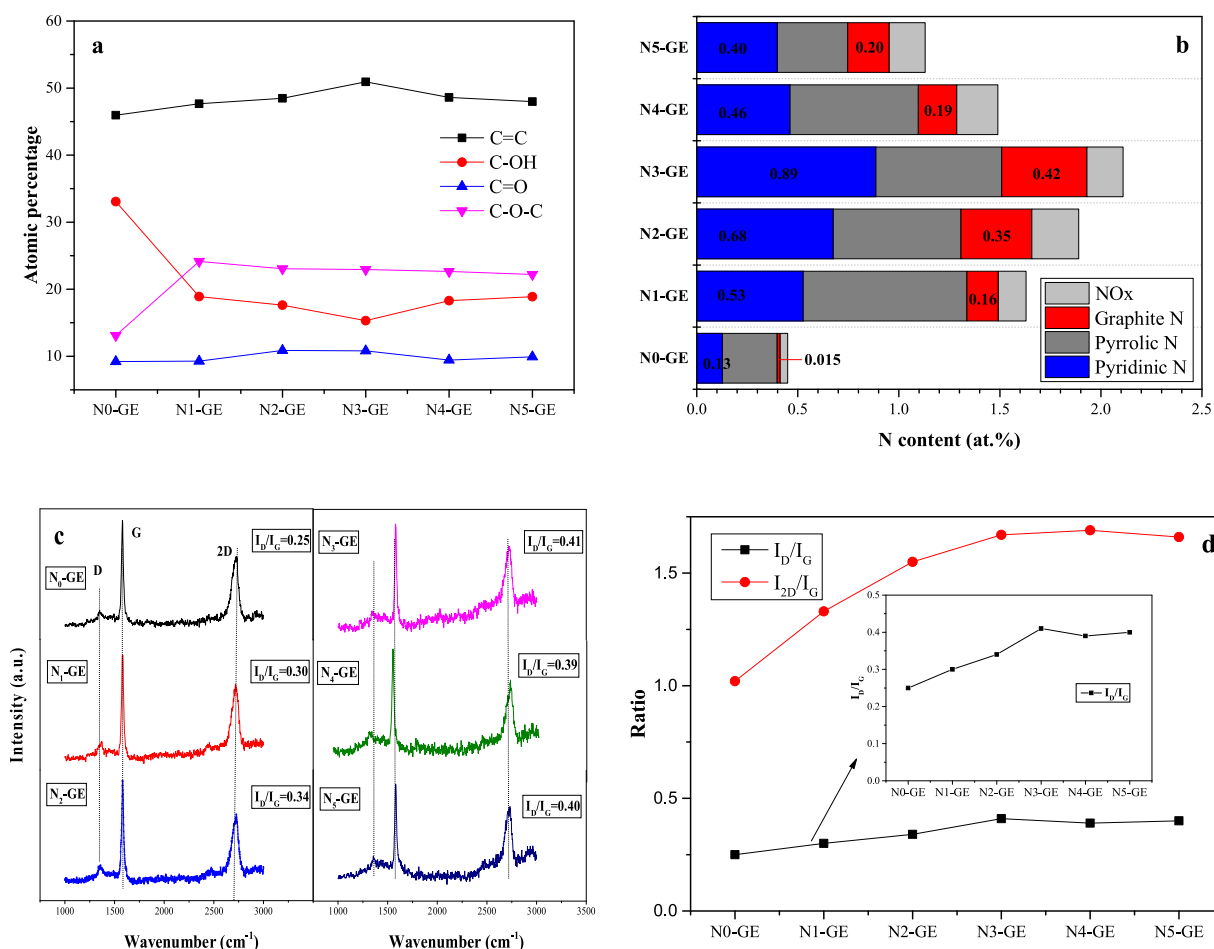


**Fig. 2.** Atomic ratio of measured by high-resolution C1s spectrum of  $N_x$ -GE (a); nitrogen species measured by N1s spectrum (b); Raman spectrum of  $N_x$ -GE (c) and ratio of change from D, G and 2D value (d).

**Table 1**

Atomic percentage in the catalyst of  $N_x$ -GE.

Sample	C1s	O1s	N1s				C/O
			Pyrrylic N	Pyridinic N	Graphite N	NO <sub>x</sub>	
N <sub>0</sub> -GE	92.17	7.38	60.20	28.25	3.29	8.25	12.49
N <sub>1</sub> -GE	93.91	4.46	49.69	32.33	9.51	8.46	21.06
N <sub>2</sub> -GE	95.22	2.89	33.46	35.73	18.54	12.26	32.95
N <sub>3</sub> -GE	95.04	2.85	29.49	42.02	20.01	8.47	33.35
N <sub>4</sub> -GE	94.62	3.89	42.59	30.99	12.78	13.64	24.32
N <sub>5</sub> -GE	95.47	3.40	30.80	35.30	18.20	15.70	28.08

For the quantitative determination of  $\cdot\text{OH}$  from cathode, dimethyl sulfoxide (DMSO), 2, 4-dinitrophenylhydrazine (DNPH), and phosphate buffer solutions (pH = 4) were used to produce hydrazine to further quantify the  $\cdot\text{OH}$  [52].

## 2.5. Pollutants degradation by in-situ metal-free EAOPs and EF

The phenol and some intermediates were mainly analyzed by HPLC (Ultimate 3000) equipped with C18 column ( $\phi 3.0 \times 100$  mm) at 0.3 mL/min, using a mobile phase of methanol: water: glacial acetic acid (v/v/v 30:19:1). Carboxylic acids were measured by HPLC with a HPX-87H ion exclusion column ( $6 \mu\text{m}$ ,  $7.8 \text{ cm} \times 300$  mm) performing at  $55^\circ\text{C}$ . The detector was a UV detector at wavelength of 210 nm, and the mobile phase was 2.5 mM  $\text{H}_2\text{SO}_4$  at flow rate of 0.4 mL/min. TOC was monitored by a TOC analyzer (Analytikjena multi N/C 3100, Germany) to illustrate the degree of mineralization during

contaminants degradation. Mineralization current efficiency (MCE) was calculated by the following formula [51]:

$$\text{MCE}(\%) = \frac{nFV\Delta(\text{TOC})_{\text{exp}}}{4.32 \times 10^7 mIt} \times 100 \quad (8)$$

Where  $n$  is the electrons consumed per phenol molecule during its mineralization,  $F$  is the Faraday constant,  $V_s$  is the bulk volume (L),  $\Delta(\text{TOC})_{\text{exp}}$  is the TOC decay (mg/L),  $4.32 \times 10^7$  is the conversion factor ( $3600 \text{ s/h} \times 1200 \text{ mg/mol}$ ),  $m$  represents the number of carbon atoms of phenol,  $I$  is current (I) and  $t$  represents time (h).

Methylene blue (MB) and rhodamine B (RhB) was measured using spectrophotometer at wavelength of 664 nm and 554 nm, respectively. The detection of *p*-nitrophenol (PNP) was almost the same as that for phenol except the detector wavelength at 317 nm. The tetracyclines (TC) and oxytetracycline (OTC) were analyzed by HPLC equipped with an ACQUITY UPLC BEH C18 column ( $1.7 \mu\text{m}$ ,  $\phi 2.1 \times 100$  mm) and a diode array detector, operating with the mobile phase of acetonitrile: formic acid (0.1 M) (v/v, 3:7) at the flow rate of 0.14 mL/min.

## 3. Results and discussion

### 3.1. Materials characterization

When mixture of CB and GE was coated on carbon felt, the SEM image of CB-GF, GE(CB)-GF, and N-GE(CB)-GF were shown in Fig. S2, observing no significant changes in carbon black and graphene. And XPS spectra of CB, the mixture of CB and GE, GE(CB)-GF and N-GE (CB)-GF were analyzed (Fig. S3). Due to the lower content of nitrogen,

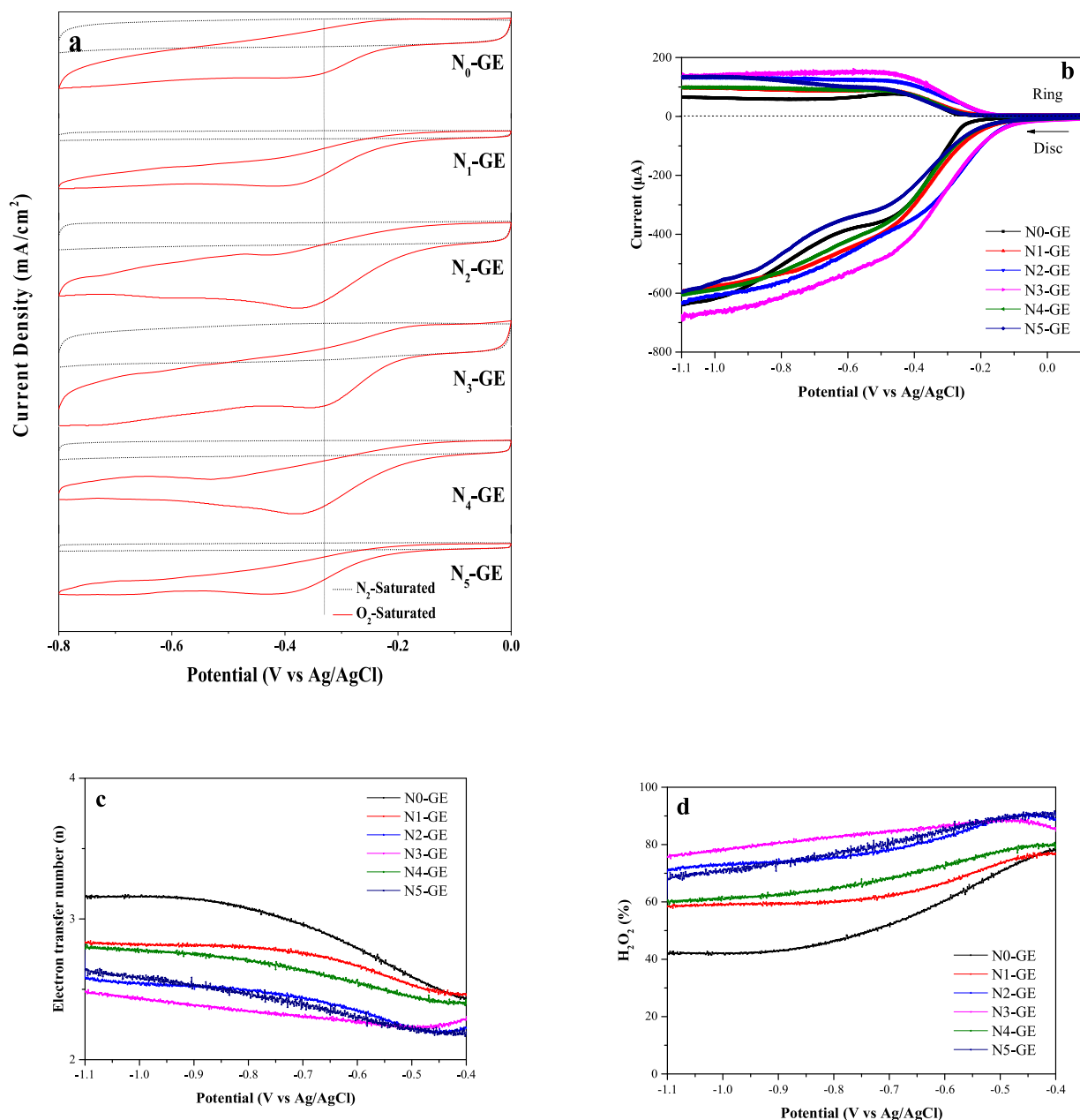


**Fig. 3.** CV in N<sub>2</sub>/O<sub>2</sub>-saturated 50 mM Na<sub>2</sub>SO<sub>4</sub> (a); disk current and ring current of RRDE tests at 900 rpm (b); electron transfer number (c) and H<sub>2</sub>O<sub>2</sub> yield of N<sub>x</sub>-GE (d).

**Table 2**  
Electrochemical parameters for the ORR estimated from CV and LSV.

materials	Disk onset potential (V vs Ag/AgCl)	reduction peaks	Disk current (μA) at -1.1 V vs Ag/AgCl	Number of electrons	%H <sub>2</sub> O <sub>2</sub>
N <sub>0</sub>	-0.236	–	640	3.15	42.22
N <sub>1</sub>	-0.155	-0.421	614	2.83	58.36
N <sub>2</sub>	-0.191	-0.378	624	2.58	70.92
N <sub>3</sub>	-0.054	-0.356	676	2.49	75.79
N <sub>4</sub>	-0.174	-0.380	605	2.79	60.14
N <sub>5</sub>	-0.166	-0.433	569	2.62	68.54

the response of introduced N element was not obvious. Therefore, when analyzing the properties of the introduced N element later, only N<sub>x</sub>-GE was analyzed without analysis of mixture of CB and N<sub>x</sub>-GE.

The SEM image demonstrated that both N-GE (Fig. 1a) and GE (insert Fig. 1a) were folded laminar structure, but N-GE showed smoother surface and less agglomeration. The TEM image also revealed that N-GE displayed a crumpled, cross-linked structure (Fig. 1b) with 4–5 thin layers (insert Fig. 1b). As shown in Fig. 1c–e, the elemental mapping images revealed that N-GE catalysts included C, O and N, which were homogeneously distributed in the graphene structure. The contents of C, O, and N in the EDX pattern (Fig. 1f) were 96.85%, 2.17%, and 0.98%, respectively, indicating that N had been successfully doped into the graphene.

The chemical composition of N<sub>x</sub>-GE was characterized by XPS (Fig. S4), observing the peak of C1s (284 eV), N1s (399 eV), and O1s (531 eV), respectively. In the C1s spectrum (Fig. S5), the peaks could be attributed to four dominant bonds of C=C, C–OH, C–O–C/C=N and C=O/C–N [24,53–55], respectively. The existence of C=N and C–N bonding was observed from Fig. S6 (see details the analysis in supporting information) [56–59]. As shown in Fig. 2a, C=C group reached

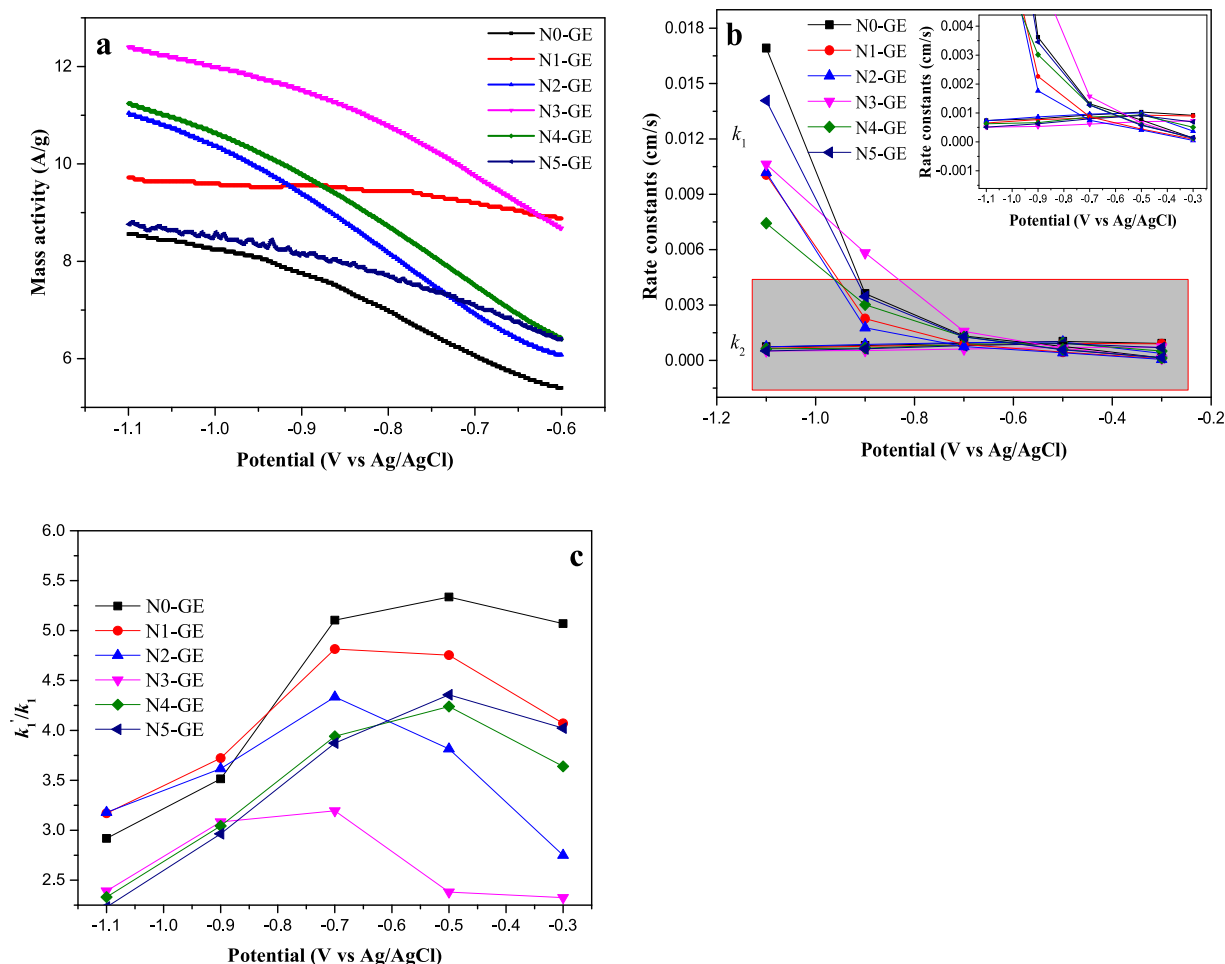


Fig. 4. Mass activity of N<sub>x</sub>-GE (a); the rate constants of the value of  $k_1$  and  $k_2$  (b); the rate constants of the value of  $k_1/k_1$  (c).

the maximum (50.94%) in N<sub>3</sub>-GE, which was the main component of sp<sup>2</sup> carbon atoms that would facilitate the ORR activity of 2e<sup>-</sup> process [35,60,61]. The N1s spectrum (Fig. S7) was further deconvoluted into four typical peaks of N1s mainly including pyrrolic N, graphite N, pyridinic N and NO<sub>x</sub> [62,63]. As the proportion of melamine increased, the N content also increased and reached a maximum at N<sub>3</sub>-GE (2.11%), and then decreased again (Table 1 and Fig. 2b). This also indicated that N was more susceptible to be oxidized and removed during the activation process, resulting in a decrease of N content [64–66]. Graphite N and pyridinic N had the same tendency as N content, while pyrrolic N had the opposite trend (Fig. 2b).

Fig. 2c shows the Raman spectrum of N<sub>x</sub>-GE. The bands of 1350, 1582 and 2680 cm<sup>-1</sup> represented the D, G and 2D bands, respectively. It was reported that the D band was related to the sp<sup>2</sup> hybrid carbon atom, showing a certain defect structure and disorder [67–69]. The I<sub>D</sub>/I<sub>G</sub> value of the N<sub>3</sub>-GE was 0.41, and as the doping amount increased, the D/G value remained unchanged (Fig. 2d), suggesting that N<sub>3</sub>-GE had the largest defects density [67,70]. Although the I<sub>D</sub>/I<sub>G</sub> value was low, it indicated that N<sub>x</sub>-GE remained high crystalline quality [71]. As seen in Table 1 and Fig. 2d, the higher the C/O ratios, the higher the degree of graphitization, which was consistent with literature [62]. The 2D/G ratio of 1.67 showed that N<sub>3</sub>-GE had few layer numbers. As layers increased, the symmetry and the ratio both decreased [60,70].

### 3.2. Electrochemical measurements of N<sub>x</sub>-GE

In the CV curve of N<sub>0</sub>, the reduction peak was not obvious, but after N doping, the reduction peak intensity was significantly enhanced

(Fig. 3a). The peak potential of the N<sub>3</sub>-GE was more positive (-0.356 V vs. Ag/AgCl) than the other samples, indicating that O<sub>2</sub> was more easily reduced on N<sub>3</sub>-GE. As depicted in Fig. 3b and RRDE test result (Table 2), the N<sub>3</sub>-GE exhibited a more positive onset potential (-0.054 V) and larger disk current (-1.1 V vs Ag/AgCl, 676 μA) than other N<sub>x</sub>-GE catalysts. According to the relationship between disk current and ring current, the  $n$  and H<sub>2</sub>O<sub>2</sub> selectivity could be obtained in Fig. 3c and d. The calculated  $n$  for N<sub>0</sub> was 3.15, indicating 2e<sup>-</sup> and 4e<sup>-</sup> reaction were simultaneously occurred in the ORR process. After N doping,  $n$  (-1.1 V) was all less than 3 for N<sub>x</sub>-GE (1–5), showing that 2e<sup>-</sup> pathway was dominant in ORR process. The H<sub>2</sub>O<sub>2</sub> selectivity of N<sub>0</sub> was 42.22%, and H<sub>2</sub>O<sub>2</sub> selectivity of N<sub>x</sub>-GE (1–5) was enhanced to 58.36%, 70.92%, 75.79%, 60.14% and 68.54%, respectively.

According to RDE results (Fig. S8), the mass activity of N<sub>x</sub>-GE at a given applied potential could be obtained [35], which was observed to increase as the potential increased (Fig. 4a). And the mass activity of N<sub>3</sub>-GE ranked the highest (12.4 A/g at -1.1 V) among all N<sub>x</sub>-GE, indicating that the most active sites were accessible. It also suggested that potential of -1.1 V would be more conducive to H<sub>2</sub>O<sub>2</sub> production and pollutants removal.

To further explore the possible ORR kinetics of N<sub>x</sub>-GE, the schematic diagram of kinetics in ORR process was illustrated in supporting information [49]. As shown in Fig. 4b,  $k_1$  values decreased with potential decreasing for all N<sub>x</sub>-GE. Besides, the values of  $k_2$  were approximately zero compared with  $k_1$ , which demonstrated the process that conversion of H<sub>2</sub>O<sub>2</sub> to H<sub>2</sub>O could be negligible. However, when the potential was -0.5 V and -0.3 V, the values of  $k_2$  were greater than the values of  $k_1$ , indicating the process of  $k_2$  was not negligible when the potential

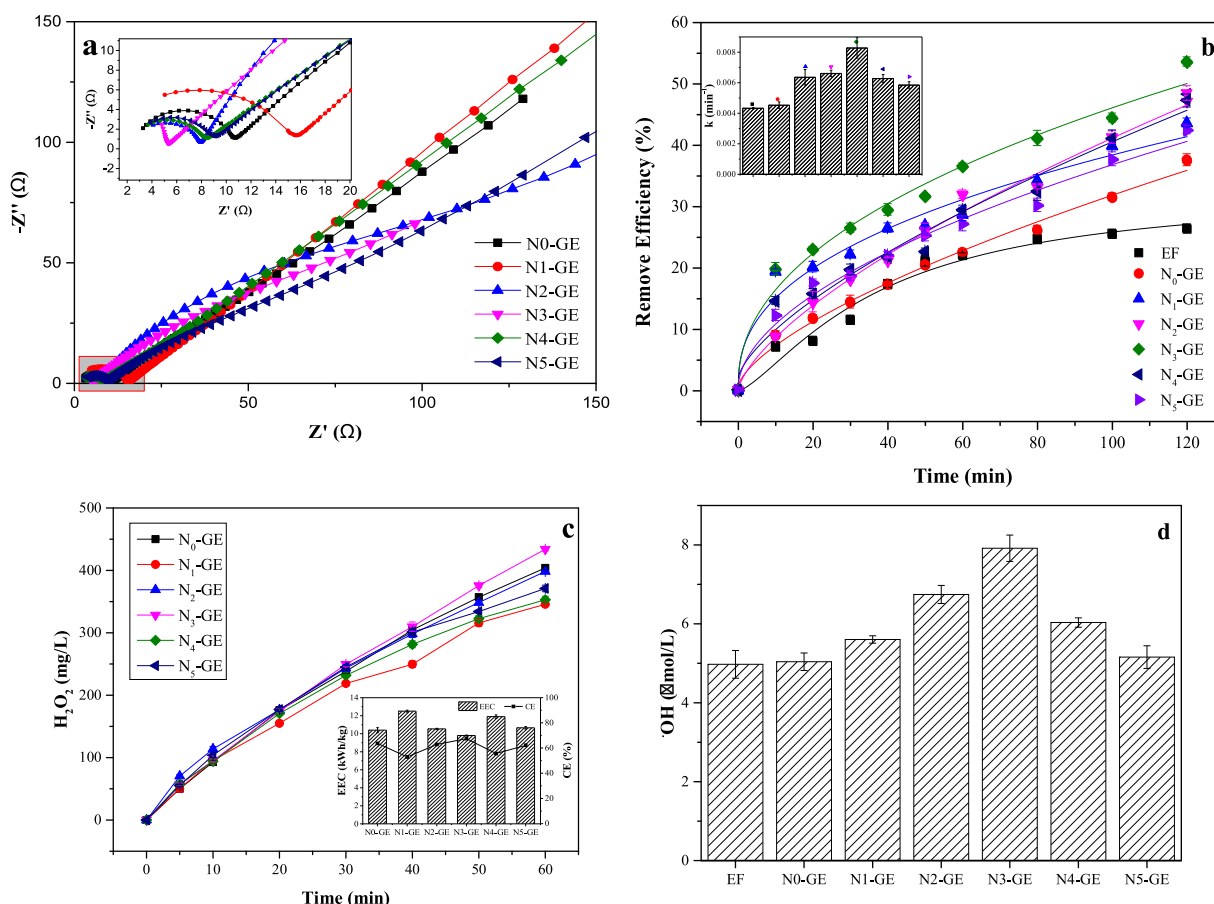


**Fig. 5.** Nyquist plot of the  $N_x$ -GE-GF (a), phenol removal (b) and the performances of  $H_2O_2$  generation (c) and  $\cdot OH$  (d) of  $N_x$ -GE-GF electrodes; Conditions: potential: -1.1 V; pH = 7; initial concentration of phenol: 50 mg/L;  $Na_2SO_4$  = 50 mM, V = 100 mL;  $V_{air}$  = 0.75 L/min.

was closer to 0. It was seen from Fig. 4c that after N doping the values of  $k_1'/k_1$  were lower than that of  $N_0$ , and the value of  $k_1'/k_1$  of  $N_3$ -GE was almost the smallest at different potentials. This fact was in agreement with the best  $H_2O_2$  selectivity for  $N_3$ -GE as observed in Fig. 3d.

### 3.3. Performances of $N_x$ -GE-GF and doping contribution

As the Nyquist plot of the  $N_x$ -GE-GF shown in Fig. 5a and Table S1, the  $N_3$ -GE-GF displayed the smallest three resistances and total resistance in the low frequency region, indicating that it could contribute to the highest electrochemical performance.

Since the suitable pH range was limited in EF, the performance of  $N_x$ -GE-GF by in-situ metal-free EAOPs under neutral conditions (pH = 7) were investigated. The removal efficiency of phenol (50 mg/L) for  $N_x$ -GE-GF (1–5) reached 43%, 47%, 54%, 48%, and 42%, respectively, which was all more efficient than that of conventional EF (26%) (Fig. 5b). The phenol degradation was found obeying a pseudo-first-order kinetics, and the reaction rate constant ( $k_{app}$ ) of  $N_3$ -GE-GF was highest (0.0083 min<sup>-1</sup>) (insert Fig. 5b). This performance was also compared with other AOPs with added  $H_2O_2$  (e.g., UV/ $H_2O_2$ ,  $O_3$ / $H_2O_2$ ,  $H_2O_2$  and EF (Table S2). Although the rate constants by  $O_3$ / $H_2O_2$  and UV/ $H_2O_2$  were larger, the energy consumption (EE/O) required was 31.7 times and 6.30 times of the present work, respectively. This fact supported that the present in-situ metal-free EAOPs were promising for environmental application.

Under this pH condition, the difference on the observed  $H_2O_2$  yield of  $N_x$ -GE was small, and the  $H_2O_2$  yield for  $N_3$ -GE-GF (8.6 mg/h/cm<sup>2</sup>) was slightly higher than that of  $N_0$ , and EEC was also the lowest (9.8 kWh/kg) (Fig. 5c). Although the  $H_2O_2$  yield on carbon nanotube

was about twice that of  $N_3$ -GE, the EEC was also increased accordingly in literature. When tungsten oxide was used to modify carbon material, the  $H_2O_2$  yield could reach 27.9 mg/h/cm<sup>2</sup>, but the CE was only 41.9%. And when graphene was used as a cathode in other literatures, the performance of  $H_2O_2$  production was much lower than the present work. Therefore, accounting for the  $H_2O_2$  yield, CE and EEC,  $N_3$ -GE exhibited almost the best among the literature using different carbon materials (Table S3).

This disagreement between phenol degradation performance and  $H_2O_2$  yields indicated that these should be other active species determining the degradation reactions. Therefore, a series of scavenger experiments using methanol ( $\cdot OH$  and  $\cdot SO_4^-$  capturer) [72,73], benzoquinone (BQ,  $O_2^{\cdot -}$  capturer) [74], or *tert*-butanol (TBA,  $\cdot OH$  capturer) [75–77] were carried out using  $N_3$ -GE-GF as the cathode for phenol degradation (Fig. S9). Obviously, when methanol was added, the removal efficiency of phenol decreased from 53.47% to 14.43%, and when TBA was added, it dropped to 14.96%, indicating the contribution of  $\cdot SO_4^-$  to phenol removal was ignorable. However, when BQ was added to capture  $O_2^{\cdot -}$ , the removal efficiency reduced to 43.09%. This phenomenon showed that  $\cdot OH$  played the most important role in the degradation of phenol. Quantitatively, the contribution of  $\cdot OH$  was calculated to be 80.73% and  $O_2^{\cdot -}$  was 19.28% for phenol removal according to apparent kinetic reaction rate constant (see details the calculation in supporting information and Fig. S10).

Therefore, the concentrations of  $\cdot OH$  generated on different  $N_x$ -GE-GF cathodes were detected (Fig. 5d), which was found well fit with the tendency of those of phenol degradations (Fig. 5b). Specially, the concentration of  $\cdot OH$  with  $N_3$ -GE-GF was the highest, which was about 1.5 times that of EF at 2 h. These facts confirmed that the catalytic conversion of electrochemically generated  $H_2O_2$  to  $\cdot OH$  was the key to

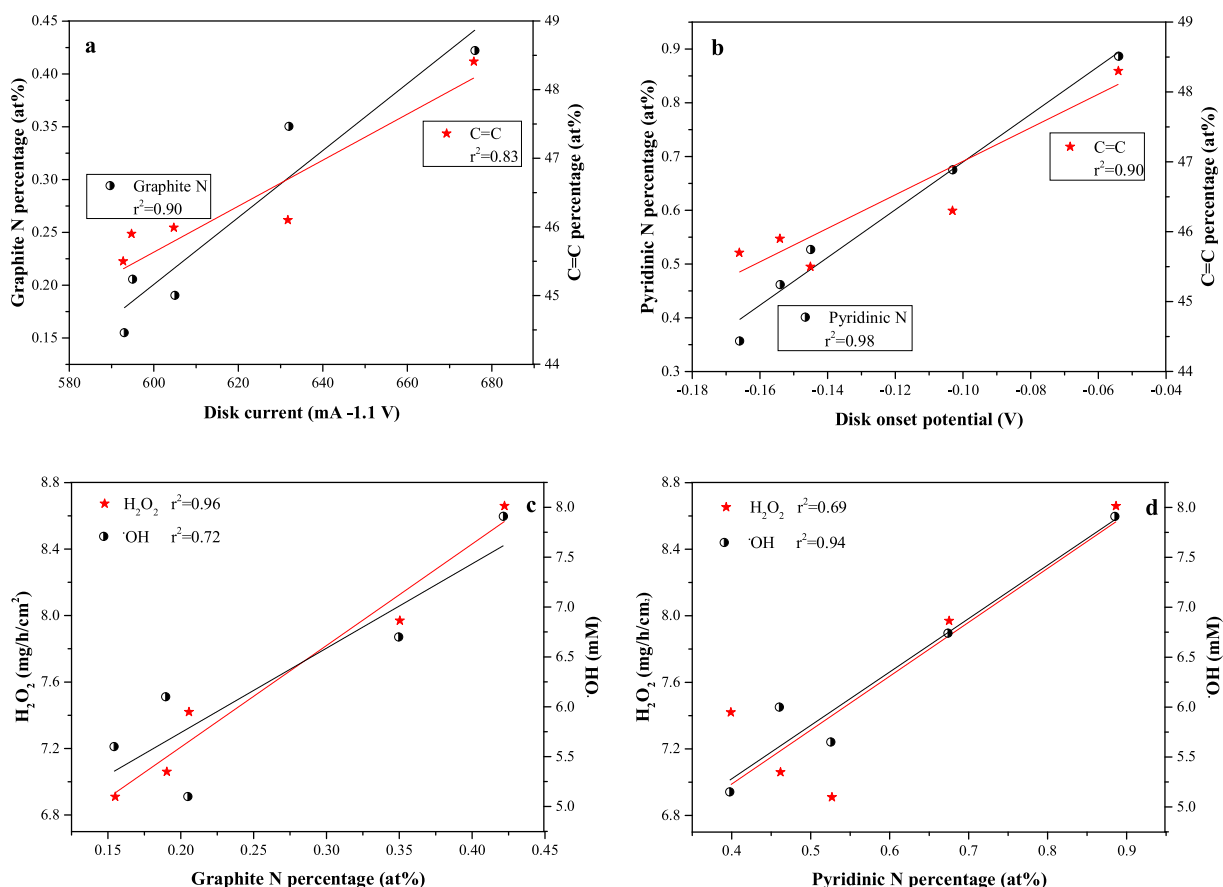


Fig. 6. Relationship between current and the C = C or graphite N (a); Relationship between onset potential and the C = C or pyridinic N (b); Relationship between yield of  $\text{H}_2\text{O}_2$  and concentration of  $\cdot\text{OH}$  with graphite N (c), pyridinic N (d).

the organic pollutant degradation. By calculating  $k_3$  and  $k_3/k_1$  in ORR process based on the concentration of  $\text{H}_2\text{O}_2$  and  $\cdot\text{OH}$ , it could be found that the ability of  $\text{N}_3\text{-GE}$  catalyzing  $\text{H}_2\text{O}_2$  to  $\cdot\text{OH}$  was the most effective among all  $\text{N}_x\text{-GE}$  (Table S4). Also it indicated the catalysis of  $\text{H}_2\text{O}_2$  to  $\cdot\text{OH}$  was much slower than that of  $\text{H}_2\text{O}_2$  generation, which led to the accumulation of  $\text{H}_2\text{O}_2$ . The results of phenol removal in Fig. 5b, and  $\text{H}_2\text{O}_2$  and  $\cdot\text{OH}$  concentration in Fig. 5c and d indicated that  $\text{H}_2\text{O}_2$  yield and phenol removal were higher due to the increase of active sites in  $\text{N}_3\text{-GE}$ .

To further explore why  $\text{N}_3\text{-GE-GF}$  performed the best and what might be active sites that driven the catalysis of  $\text{H}_2\text{O}_2$  to hydroxyl radical, the relationship between current, onset potential and active species production with doping elemental contents were investigated. As can be seen in Fig. 6a and b, the content of C = C affected the onset potential in RRDE thereby affecting the catalytic activity, while the effect on the disk current (-1.1 V) was relatively smaller. This result was also consistent with the results of XPS that the contents of C = C affected ORR activity.

The nitrogen content had a significant effect on ORR catalytic activity. Gao et al. [45] thought that a higher percentage of the active pyridinic N and graphite N was beneficial for enhancing the ORR activity. Most importantly, graphite N was the main active sites to produced  $\text{H}_2\text{O}_2$  in  $2\text{e}^-$  pathway and pyrrolic N sites mainly influenced  $4\text{e}^-$  pathway in ORR [46,78]. In the  $2\text{e}^-$  ORR process, the content of graphite N mainly determined the current (Fig. 6a), while the content of pyridinic N could improve the onset potential for catalysts (Fig. 6b), which was consistent with the result of  $4\text{e}^-$  ORR in the literatures [79,80]. Therefore, the  $\text{N}_3\text{-GE}$  with the highest content of reactive nitrogen species (62.03 at. %) had the promising potential to improve the ORR performance.

Tan et al. [81] measured intermediate in ORR process to discuss chemical composition change of N-doped graphene, and found pyridinic N was catalytic active sites. The relationship between  $\text{H}_2\text{O}_2$  yield,  $\cdot\text{OH}$  concentration and contents of N are shown in Fig. 6c and d, respectively. The relationship between the yield of  $\text{H}_2\text{O}_2$  and graphite N was linearly positive after N doping. However, the linear relationship between the content of graphite N and the concentration of  $\cdot\text{OH}$  was poor (Fig. 6c). This phenomenon showed that graphite N had a certain linear effect on the production of  $\text{H}_2\text{O}_2$ , but the effect on catalyzing  $\cdot\text{OH}$  generation was less. However, the influence of pyridinic N on the  $\text{H}_2\text{O}_2$  yield and the  $\cdot\text{OH}$  concentration was the opposite for graphite N. There was a better linear relationship between pyridinic N and concentration of  $\cdot\text{OH}$  compared to the  $\text{H}_2\text{O}_2$  yield (Fig. 6d). This result proved that the presence of pyridinic N could catalyze  $\text{H}_2\text{O}_2$  to form  $\cdot\text{OH}$ .

### 3.4. Phenol degradation behaviors under different conditions by $\text{N}_3\text{-GE-GF}$

Operation parameters such as initial phenol concentration, applied potential and pH affect the degradation behaviors. As shown in Fig. 7a, phenol of initial concentration of 10–25 mg/L could be completely degraded on  $\text{N}_3\text{-GE-GF}$  cathode within 120 min at pH 7. For 30 mg/L phenol, the removal efficiency was 80.04%, while for 50 mg/L phenol, it was only 53.47%. It was not surprised that the higher the initial concentration, the lower the degradation rate constant (Fig. S11) due to the limitation on  $\cdot\text{OH}$  generation.

To explore the effect of cathode potential, both the degradation of phenol and the generation of  $\text{H}_2\text{O}_2$  was carried out at -1.1 V, -0.9 V, -0.7 V and -0.5 V. A higher cathode potential enhanced the phenol degradation, performing the best at -1.1 V (Fig. 7b). At this cathode potential of -1.1 V (vs SCE, or -0.44 V vs RHE), the reduction condition



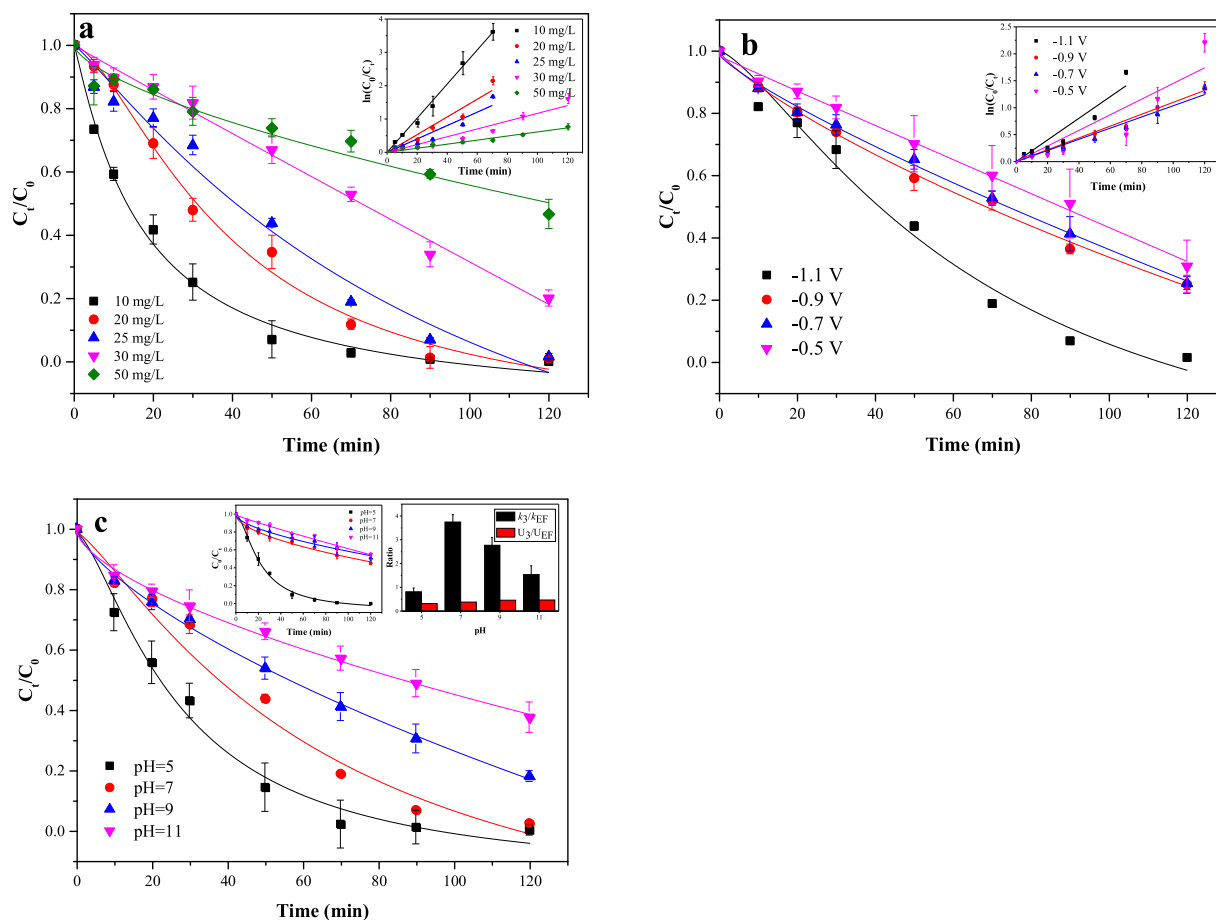


**Fig. 7.** The influence of the initial concentration of pollutants (a), Conditions: potential: -1.1 V; pH = 7; and the influence of cathode potential for phenol removal (b); Conditions: initial concentration of phenol: 25 mg/L; and the influence of pH for phenol removal (c); Conditions: initial concentration of phenol: 25 mg/L; potential: -1.1 V; (EF:  $\text{Fe}^{2+} = 0.4 \text{ mM}$ ).

was provided for  $\text{H}_2\text{O}_2$  production in  $2\text{e}^-$  ORR. Moreover, the oxidation potential of  $\cdot\text{OH}$  is 2.80 V (vs RHE) [82]. Therefore, it would provide sufficient oxidation environment for  $\cdot\text{OH}$  to degrade pollutants, which was also proved by the good performance of phenol degradation. The result of potential should be attributed to the generation of  $\text{H}_2\text{O}_2$ , which was also found increasing with the enhancement of the cathode potential (Fig. S12). At the potential of -1.1 V, the concentration of  $\text{H}_2\text{O}_2$  reached 682.95 mg/L at 120 min, and the EEC was also the smallest. It was shown in Fig. 7b that -1.1 V (vs SCE) of cathode potential was beneficial to  $\text{H}_2\text{O}_2$  production and phenol removal, and they became lower when the cathode potential decreased, which were consistent with the results in Fig. 4a.

The effect of pH on the phenol degradation by in-situ metal-free EAOPs of  $\text{N}_3\text{-GE-GF}$  was investigated and compared with EF (Fig. 7c). As literature reported [8,83], EF is highly pH dependent, and the performance was found greatly declined after pH higher than 7 when comparing with that of pH at 5 in our work (insert Fig. 7c). Comparably, the degradation of phenol by in-situ metal-free EAOPs was less affected by pH than that of EF, though it was also decreased with enhanced pH since acidic conditions was supposed to be more favorable for  $\cdot\text{OH}$  oxidation. At pH neutral and alkaline conditions, the degradation rate constants of in-situ metal-free EAOPs were much higher than that by EF (i.e.,  $k_{app-3}/k_{app-EF} > 1$ ), while the EEC ratio ( $\text{EEC}_3 / \text{EEC}_{EF}$ ) were all less than 0.5, suggesting that this in-situ metal-free EAOPs was more cost-effective than that of EF.

### 3.5. Catalytic mechanism by N-GE

To further explore the possible mechanism difference between EF and in-situ metal-free EAOPs, the degradation intermediates of phenol were identified (Fig. 8). It could be found that the concentration of hydroquinone reached the maximum at 50 min by in-situ metal-free EAOPs, which was much later than the EF (10 min). And the time reaching maximum for catechol was exactly the opposite of hydroquinone by in-situ metal-free EAOPs (10 min) and EF (50 min). The maximum concentration of catechol was almost the same in the two processes, but the concentration of hydroquinone by in-situ metal-free EAOPs was 1.42 times that by EF.

The main carboxylic acids products by two processes were identified to be glyoxylic acid, maleic acid, formic acid and fumaric acid, and their concentration in EF was all higher than that in-situ metal-free EAOPs (Fig. 8b and c). Succinic acid was also detected by in-situ metal-free EAOPs, but not in EF. The glyoxylic acid concentration was higher, reaching the highest (0.38 mM) at 10 min, then decreased rapidly and disappeared at 3 h in EF. But by in-situ metal-free EAOPs, it formed less (0.2 mM) but took a longer time of 6 h to vanish. In EF, the concentration of formic acid was approximately 10 times that of in-situ metal-free EAOPs, and the removal of formic acid in EF was also faster and finally the remaining concentration was about half that of in-situ metal-free EAOPs. The residual concentration of succinic acid by in-situ metal-free EAOPs process was about 1/4 of the initial concentration. After 2 h, the TOC removal efficiency was 25% and 32% for EF and in-situ metal-free EAOPs, respectively (Fig. 8d). The probable reason was that the concentration of catechol in EF was higher and concentration

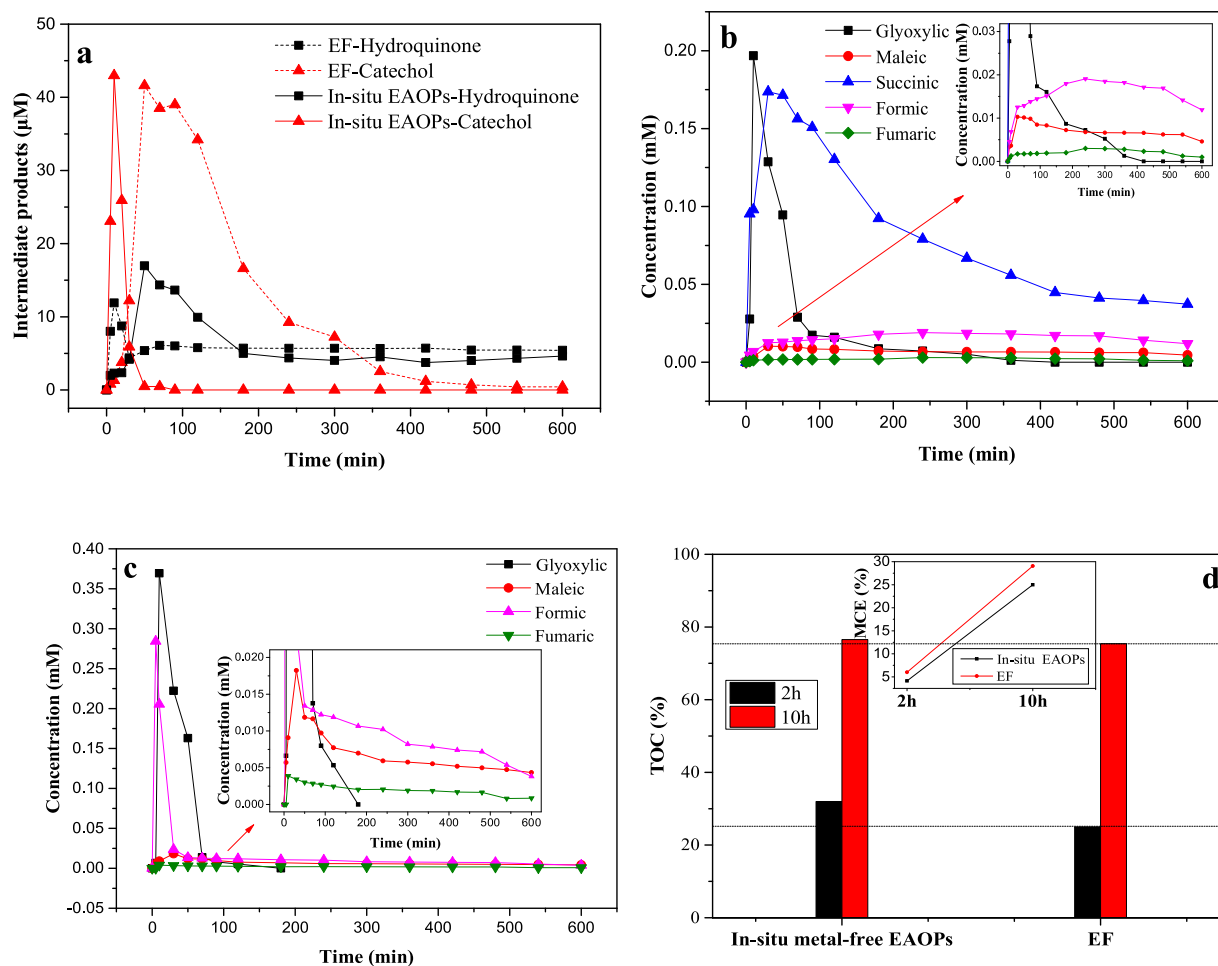


**Fig. 8.** Evolution of hydroquinone and catechol (a) for EF and in-situ metal-free EAOPs; and evolution of carboxylic acids formed by in-situ metal-free EAOPs (b) and EF (c); the TOC removal efficiency at 2 h and 10 h during oxidation of phenol. Conditions: phenol = 25 mg/L, potential = -1.1 V; pH = 7; (EF:  $\text{Fe}^{2+}$ : 0.4 mM).

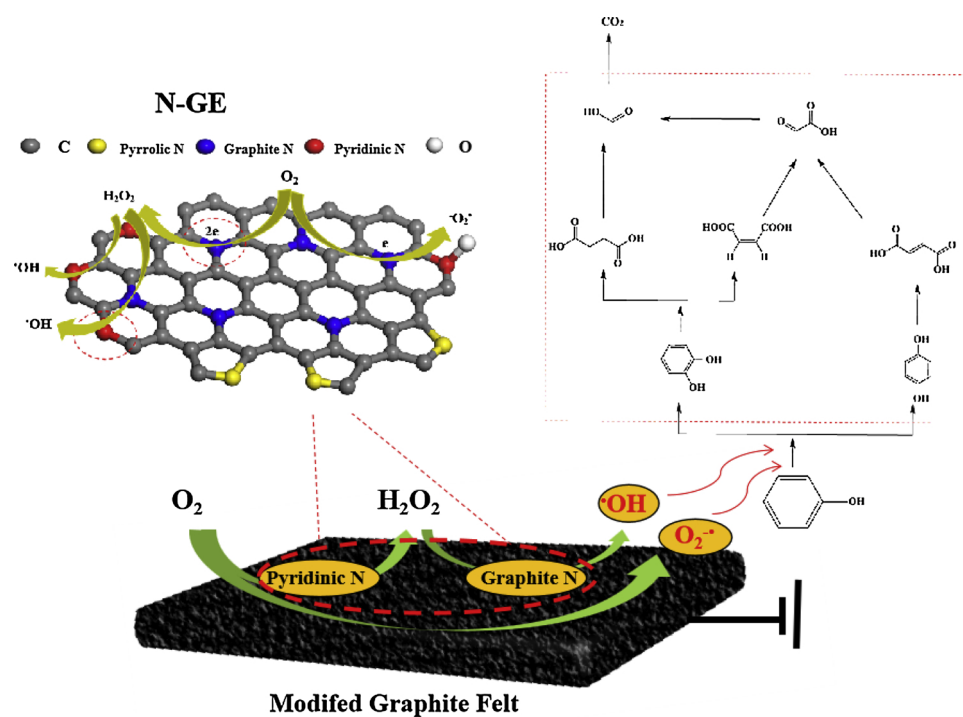


**Fig. 9.** Schematic illustration of the in-situ metal-free EAOPs and the possible removal pathway of phenol with N<sub>3</sub>-GE-GF.

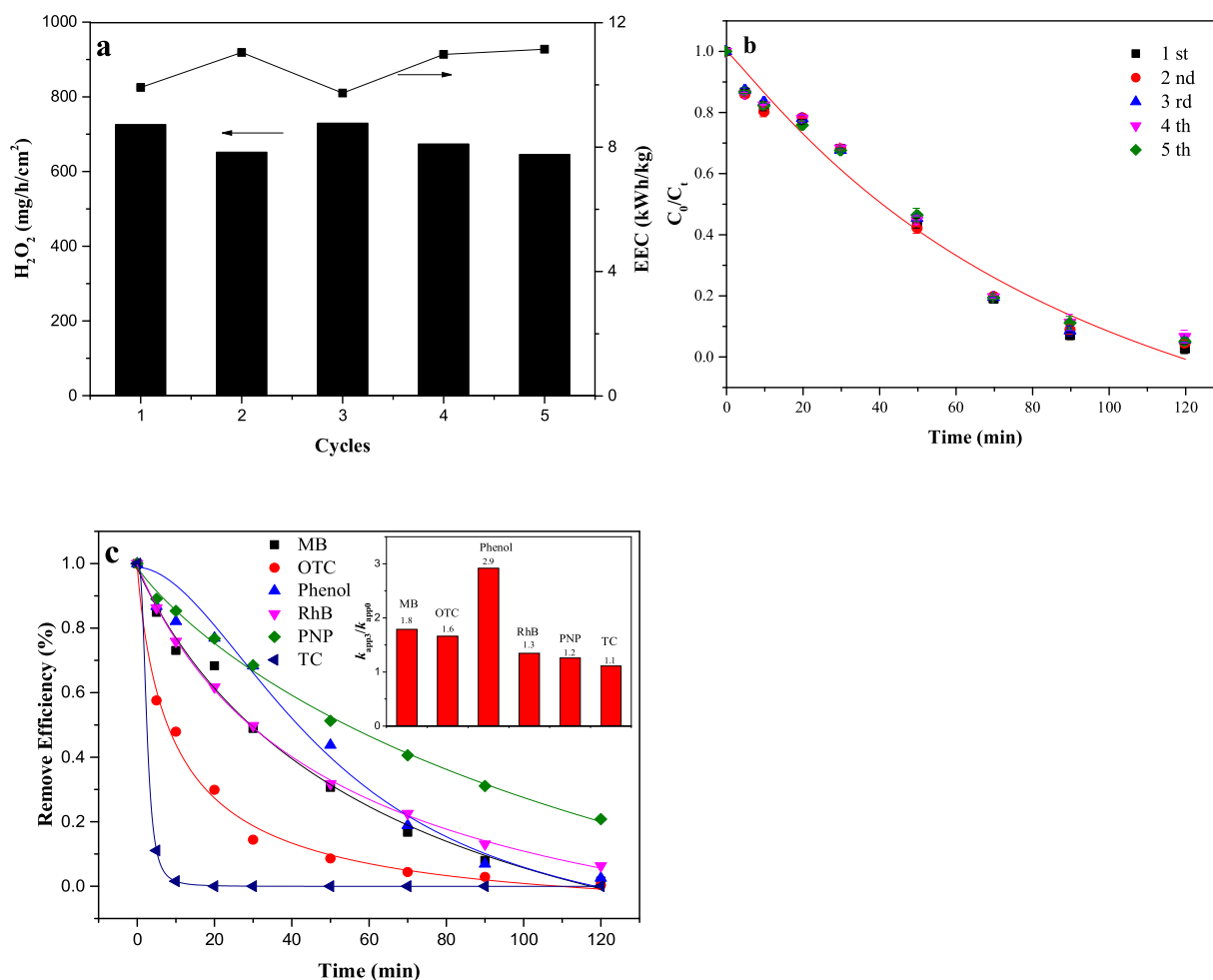


**Fig. 10.** Stability of the modified cathode with N<sub>3</sub>-GE-GF over 5 cycles for the yield of H<sub>2</sub>O<sub>2</sub> and EEC (a); phenol removal (b); Degradation of different pollutants (c). Conditions: pH = 7; Potential: -1.1 V; MB = 50 mg/L, RhB/PNP = 10 mg/L, TC/OTC = 10 mg/L; phenol = 25 mg/L.

of carboxylic acid was lower at 2 h. After 10 h, the TOC removal efficiency in two processes was 76.54% and 75.40%, respectively. There was a higher residual concentration of hydroquinone in the EF process, and there was a certain amount of succinic acid residue in the in-situ metal-free EAOPs after 10 h. In summary, the phenol degradation intermediates in two process were basically similar except succinic acid, but the degradation trends were different, which might be due to the difference on mechanism by EF and in-situ metal-free EAOPs which co-existed the role of O<sub>2</sub><sup>•-</sup> oxidation [84,85].

According to the analysis above, the possible catalysis mechanism of N<sub>3</sub>-GE by in-situ metal-free EAOPs could be depicted in Fig. 9. Due to the difference of electronegativity of N (3.04) and C (2.55) atoms, N<sub>3</sub>-GE would produce positive charge sites for the O<sub>2</sub> surface adsorption and catalysis. Most of O<sub>2</sub> performed in 2e<sup>-</sup> process of ORR with H<sub>2</sub>O<sub>2</sub> generation under the influence of the graphite N. And further H<sub>2</sub>O<sub>2</sub> was activated by pyridinic N to form <sup>•</sup>OH for organics degradation. At the same time, another small part of the O<sub>2</sub> obtained electron to form O<sub>2</sub><sup>•-</sup> (Eq. (9)). However, it is still not clear whether the active sites were graphite N or pyridinic N for producing <sup>•</sup>O<sub>2</sub>, then it needs to be explored later.



After the generation of free radicals, phenol was attacked and degraded. A plausible degradation pathway of phenol was proposed based on these detected by-products by in-situ metal-free EAOPs and EF (Fig. 9 and Fig. S13) [4]. First, hydroquinone and catechol were generated from phenol. Fumaric acid was generated from hydroquinone

through cleavages of benzene ring under the action of free radicals. Maleic acid and succinic acid were generated from catechol. After, fumaric acid and maleic acid were further degraded and converted into glyoxylic acid. Then, glyoxylate and succinic acid eventually became simple formic acid, and eventually mineralized to CO<sub>2</sub>. However, catechol only produced maleic acid and no succinic acid was detected in EF.

### 3.6. Stability and performance for organic pollutants degradation

In order to explore the reusability of N<sub>3</sub>-GE-GF, the yield of H<sub>2</sub>O<sub>2</sub> and phenol removal efficiency were operated using the same modified cathode after cleaning under the same conditions in five runs. As shown in Fig. 10a, the average yield of H<sub>2</sub>O<sub>2</sub> was 691.6 mg/L at 120 min. These results indicated that the modified cathode of N<sub>3</sub>-GE-GF showed good stability and reusability for H<sub>2</sub>O<sub>2</sub> production. In EF, Fe<sup>2+</sup> cannot be reused, so the reusability of modified electrodes in-situ metal-free EAOPs for phenol removal (Fig. 10b) was studied. After a simple rinse of the cathode with deionized water, phenol removal reached 95.7%, 94.4%, 93.4%, and 95.0% for the second, third, fourth, and fifth runs, respectively. The contact angle of the cleaning electrode was almost unchanged compared with the original cathode (Fig. S14). Since the hydrophilicity of the cathode was poor, the pollutants may only stay on the surface of the electrode by in-situ metal-free EAOPs. Therefore, when the N-doped graphene modified graphite felt was applied as the cathode, the regeneration process was relatively easy and convenient.

A series of pollutants (phenol, PNP, RhB, MB, TC, OTC) were

selected as model organic contaminants to evaluate the effectiveness of N<sub>3</sub>-GE-GF cathode for in-situ metal-free EAOPs. As shown in Fig. 10c, the  $k_{app}$  of N<sub>3</sub>-GE-GF were better than that of N<sub>0</sub> for all pollutants (insert Fig. 10c). These results indicated that N<sub>3</sub>-GE-GF was more effective in catalyzing the formation of  $\cdot\text{OH}$  for degradation of pollutants after N doping.

#### 4. Conclusions

Optimized N<sub>3</sub>-GE using melamine as a nitrogen source was an active catalytic material for generating high H<sub>2</sub>O<sub>2</sub> yield and high selectivity, and efficiently catalyzing H<sub>2</sub>O<sub>2</sub> to form  $\cdot\text{OH}$  for organic pollutants degradation by in-situ metal-free EAOPs, which were certified to be less affected by initial pH and the regeneration process was relatively easy and convenient compared with EF. Unlike EF, O<sub>2</sub><sup>•−</sup> also contributed to the phenol degradation, but  $\cdot\text{OH}$  still played the major role. Therefore, N<sub>3</sub>-GE was a promising candidate instead of iron catalyst. Among N-GE, the active N (graphite N and pyridinic N) and C=C enhanced ORR activity. Importantly, the introduction of graphite N could promote the 2e<sup>−</sup> ORR process for H<sub>2</sub>O<sub>2</sub> generation, and the presence of pyridinic N could catalyze H<sub>2</sub>O<sub>2</sub> to the production of  $\cdot\text{OH}$ . In future studies, computational studies would help to indicate the impact of active sites, and the nitrogen-functional group could be selectively controlled to regulate the catalyst performance. This study shed light on the in-situ metal-free EAOPs are promising and **green** technologies for environmental remediation without catalyst addition and iron sludge generation.

#### Acknowledgements

This work was financially supported by Natural Science Foundation of China (nos. 21773129, 91545126, 21811530274 and 21273120), Key Project of Natural Science Foundation of Tianjin (no. 16JCZDJC39300), National Key Research and Development Program (2016YFC0400706), China National Water Project (2017ZX07107002), China – Czech Science and Technology Exchange Project (42-8), 111 program, Ministry of Education, China (T2017002) and Fundamental Research Funds for the Central Universities.

#### Appendix A. Supplementary data

Supplementary material related to this article can be found, in the online version, at doi:<https://doi.org/10.1016/j.apcatb.2018.12.075>.

#### References

- [1] M. Skoumal, C. Arias, P.L. Cabot, F. Centellas, J.A. Garrido, R.M. Rodríguez, E. Brillas, *Chemosphere* 71 (2008) 1718–1729.
- [2] B. Balci, N. Oturan, R. Cherrier, M.A. Oturan, *Water Res.* 43 (2009) 1924–1934.
- [3] A. Dirany, I. Sires, N. Oturan, M.A. Oturan, *Chemosphere* 81 (2010) 594–602.
- [4] M. Pimentel, N. Oturan, M. Dezotti, M.A. Oturan, *Appl. Catal. B* 83 (2008) 140–149.
- [5] H. Zhao, Y. Chen, Q. Peng, Q. Wang, G. Zhao, *Appl. Catal. B* 203 (2017) 127–137.
- [6] E. Brillas, I. Sires, M.A. Oturan, *Chem. Rev.* 109 (2009) 6570–6631.
- [7] G. Ren, M. Zhou, M. Liu, L. Ma, H. Yang, *Chem. Eng. J.* 298 (2016) 55–67.
- [8] H. Liu, C. Wang, X. Li, X. Xuan, C. Jiang, H. Cui, *Environ. Sci. Technol.* 41 (2007) 2937–2942.
- [9] W. Wang, Y. Lu, H. Luo, G. Liu, R. Zhang, *J. Acs Adv. Comput. Sci.* 7 (2017) 25627–25633.
- [10] L. Ma, M. Zhou, G. Ren, W. Yang, L. Liang, *Electrochim. Acta* 200 (2016) 222–230.
- [11] J. Tian, A.M. Olajuyin, T. Mu, M. Yang, J. Xing, *Environ. Sci. Pollut. Res. Int.* 23 (2016) 11574–11583.
- [12] X. Zhang, J. Fu, Y. Zhang, L. Lei, *Sep. Purif. Technol.* 64 (2008) 116–123.
- [13] G. Gao, Q. Zhang, Z. Hao, C.D. Vecitis, *Environ. Sci. Technol.* 49 (2015) 2375–2383.
- [14] H. Roth, Y. Gendel, P. Buzatu, O. David, M. Wessling, *J. Hazard. Mater.* 307 (2016) 1–6.
- [15] O. Iglesias, J. Meijide, E. Bocos, M.Á. Sanromán, M. Pazos, *Electrochim. Acta* 169 (2015) 134–141.
- [16] J.A. Bañuelos, A. El-Ghenymy, F.J. Rodríguez, J. Manríquez, E. Bustos, A. Rodríguez, E. Brillas, L.A. Godínez, *Electrochim. Acta* 140 (2014) 412–418.
- [17] W. Ren, D. Tang, X. Lu, J. Sun, M. Li, S. Qiu, D. Fan, *Ind. Eng. Chem. Res.* 55 (2016) 11085–11096.
- [18] C.Y. Chen, C. Tang, H.F. Wang, C.M. Chen, X. Zhang, X. Huang, Q. Zhang, *ChemSusChem* 9 (2016) 1194–1199.
- [19] E. Mousset, Z.T. Ko, M. Syafiq, Z. Wang, O. Lefebvre, *Electrochim. Acta* 222 (2016) 1628–1641.
- [20] T.X.H. Le, M. Bechelany, S. Lacour, N. Oturan, M.A. Oturan, M. Cretin, *Carbon* 94 (2015) 1003–1011.
- [21] A. Wang, J. Qu, J. Ru, H. Liu, J. Ge, Dye, *Pigment.* 65 (2005) 227–233.
- [22] E. Kusvuran, S. Irmak, H.I. Yavuz, A. Samil, O. Erbatur, *J. Hazard. Mater.* 119 (2005) 109–116.
- [23] S.K. Jang, J. Jeon, S.M. Jeon, Y.J. Song, S. Lee, *Solid. Electron.* 109 (2015) 8–11.
- [24] W. Yang, M. Zhou, J. Cai, L. Liang, G. Ren, L. Jiang, *J. Mater. Chem. A* 5 (2017) 8070–8080.
- [25] Y. Zhu, S. Murali, W. Cai, X. Li, J.W. Suk, J.R. Potts, R.S. Ruoff, *Adv. Mater.* 22 (2010) 3906–3924.
- [26] M. Vikkisk, I. Kruusenberg, U. Joost, E. Shulga, I. Kink, K. Tammeveski, *Appl. Catal. B* 147 (2014) 369–376.
- [27] T. Huang, S. Mao, M. Qiu, O. Mao, C. Yuan, J. Chen, *Electrochim. Acta* 222 (2016) 481–487.
- [28] Z. Yang, Z. Yao, G. Li, G. Fang, H. Nie, *ACS Nano* 6 (2012) 205–211.
- [29] C. Choi, S. Park, S. Woo, *ACS Nano* 6 (2012) 7084–7091.
- [30] T. Vineesh, M. Kumar, C. Takahashi, G. Kalita, S. Alwarappan, D. Pattanayak, T. Narayanan, *Adv. Energy Mater.* 5 (2015).
- [31] S. Chen, Z. Chen, S. Siahrostami, D. Higgins, D. Nordlund, D. Sokaras, T.R. Kim, Y. Liu, X. Yan, E. Nilsson, R. Sinclair, J.K. Norskov, T.F. Jaramillo, Z. Bao, *J. Am. Chem. Soc.* 140 (2018) 7851–7859.
- [32] J. Park, Y. Nabee, T. Hayakawa, M. Kakimoto, *ACS Catal.* 4 (2014) 3749–3754.
- [33] Z.W. Seh, J. Kibsgaard, C.F. Dickens, I. Chorkendorff, J.K. Norskov, T.F. Jaramillo, *Science* 355 (2017).
- [34] A. Verdager-Casadevall, D. Deiana, M. Karamad, S. Siahrostami, P. Malacrida, T.W. Hansen, J. Rossmeisl, I. Chorkendorff, I.E. Stephens, *Nano Lett.* 14 (2014) 1603–1608.
- [35] H.W. Kim, M.B. Ross, N. Kornienko, L. Zhang, J. Guo, P. Yang, B.D. McCloskey, *Nat. Catal.* 1 (2018) 282–290.
- [36] K. Qu, Y. Zheng, X. Zhang, K. Davey, S. Dai, S.Z. Qiao, *ACS Nano* 11 (2017) 7293–7300.
- [37] W. Tian, H. Zhang, Z. Qian, T. Ouyang, H. Sun, J. Qin, M.O. Tade, S. Wang, *Appl. Catal. B* 225 (2018) 76–83.
- [38] X. Fan, W.T. Zheng, J.-L. Kuo, *RSC Adv.* 3 (2013) 5498.
- [39] Y. Yang, F. He, Y. Shen, X. Chen, H. Mei, S. Liu, Y. Zhang, *Chem. Commun.* 53 (2017) 9994–9997.
- [40] W.P. Mounfield, A. Garg, Y. Shao-Horn, Y. Román-Leshkov, *Chem* 4 (2018) 18–19.
- [41] Y. Sun, S. Li, Z.P. Jovanov, D. Bernsmeier, H. Wang, B. Paul, X. Wang, S. Kuhl, P. Strasser, *ChemSusChem* 11 (2018) 3388–3395.
- [42] T.F. Liu, K. Wang, S.Q. Song, A. Brouzgou, P. Tsiakaras, Y. Wang, *Electrochim. Acta* 194 (2016) 228–238.
- [43] C. Peng, S. Zhou, X. Zhang, T. Zeng, W. Zhang, H. Li, X. Liu, P. Zhao, *Sens. Actuators B-Chem.* 270 (2018) 530–537.
- [44] W. Yang, M. Zhou, L. Liang, *Chem. Eng. J.* 338 (2018) 700–708.
- [45] S. Gao, L. Li, K. Geng, X. Wei, S. Zhang, *Nano Energy* 16 (2015) 408–418.
- [46] J. Liu, P. Song, M. Ruan, W. Xu, *Chinese J. Catal.* 37 (2016) 1119–1126.
- [47] F. Jaouen, *J. Phys. Chem. C* 113 (2009) 15433–15443.
- [48] F. Jaouen, J.-P. Dodelet, *J. Phys. Chem. C* 113 (2009) 15422–15432.
- [49] H. Zhao, L. Qian, Y. Chen, Q. Wang, G. Zhao, *Chem. Eng. J.* 332 (2018) 486–498.
- [50] S.-J. Lee, S.-I. Pyun, S.-K. Lee, S.-J.L. Kang, *Isr. J. Chem.* 48 (2008) 215–228.
- [51] X. Yu, M. Zhou, G. Ren, L. Ma, *Chem. Eng. J.* 263 (2015) 92–100.
- [52] C. Zhang, M. Zhou, G. Ren, X. Yu, L. Ma, J. Yang, F. Yu, *Water Res.* 70 (2015) 414–424.
- [53] T.X.H. Le, M. Bechlwany, J. Champavert, M. Cretin, *RSC Adv.* 5 (2015) 42536–42539.
- [54] L. Zhang, Z. Zhang, C. He, L. Dai, L. Wang, *ACS Nano* 8 (2014) 6663–6670.
- [55] S. Yang, S. Bruller, Z.S. Wu, Z. Liu, K. Parvez, R. Dong, F. Richard, P. Samori, X. Feng, K. Mullen, *J. Am. Chem. Soc.* 137 (2015) 13927–13932.
- [56] T.V. Khai, H.G. Na, D.S. Kwak, Y.J. Kwon, H. Ham, K.B. Shim, H.W. Kim, *Carbon* 50 (2012) 3806–3899.
- [57] A. Sionkowska, A. Planecka, *J. Mol. Liq.* 178 (2013) 5–14.
- [58] A. Navaee, A. Salimi, S. Soltanian, P. Servati, *J. Power Sources* 277 (2015) 268–275.
- [59] T. Maunula, J. Ahola, H. Hamada, *Appl. Catal. B* 64 (2006) 13–24.
- [60] S. Jiang, Z. Li, H. Wang, Y. Wang, L. Meng, S. Song, *Nanoscale* 6 (2014) 14262–14269.
- [61] M.S. Ahmed, Y.B. Kim, *Sci. Rep.* 7 (2017) 43279.
- [62] Y. Li, J. Yang, J. Huang, Y. Zhou, K. Xu, N. Zhao, X. Cheng, *Carbon* 122 (2017) 237–246.
- [63] Y. Cao, W. Si, Q. Hao, Z. Li, W. Lei, X. Xia, *Electrochim. Acta* 261 (2018) 206–213.
- [64] Z. Chen, D. Higgins, Z. Chen, *Carbon* 48 (2010) 3057–3065.
- [65] L. Meng, S. Park, *Mater. Chem. Phys.* 143 (2014) 1158–1163.
- [66] W. Gao, Y. Ma, Y. Zhou, H. Song, L. Li, S. Liu, *Mater. Lett.* 216 (2018) 84–87.
- [67] L. Qu, Y. Liu, J.B. Baek, L. Dai, *ACS Nano* 4 (2010) 1321–1326.
- [68] Z.-H. Sheng, H.-L. Gao, W.-J. Bao, F.-B. Wang, X.-H. Xia, *J. Mater. Chem.* 22 (2012) 390–395.
- [69] C. Xu, Y. Su, D. Liu, X. He, J. Chem. Soc. Faraday Trans. 17 (2015) 25440–25448.
- [70] N. Mahato, N. Parveen, M.H. Cho, *Mater. Express* 5 (2015) 471–479.
- [71] L. Qu, Y. Liu, J. Baek, L. Dai, *ACS Nano* 4 (2010) 1321–1326.
- [72] S.H. Kang, W. Choi, *Environ. Sci. Technol.* 43 (2009) 878–883.
- [73] L. Jiang, Y. Zhang, M. Zhou, L. Liang, K. Li, *J. Hazard. Mater.* 358 (2018) 53–61.
- [74] J.H. Kou, Z.S. Li, Y.P. Yuan, H.T. Zhang, Y. Wang, Z.G. Zou, *Environ. Sci. Technol.* 43 (2009) 2919–2924.



- [75] A. Sarkar, S. Kapoor, T. Mukhejee, Res. Chem. Intermed. 31 (2005) 845–856.
- [76] X. Li, M. Zhou, Y. Pan, L. Xu, Chem. Eng. J. 307 (2017) 1092–1104.
- [77] Y. Pan, Y. Zhang, M. Zhou, J. Cai, X. Li, Y. Tian, Chem. Eng. J. 354 (2018) 777–789.
- [78] D. Guo, R. Shibuya, C. Akiba, S. Saji, T. Kondo, J. Nakamura, Science 351 (2016) 361–365.
- [79] L. Lai, J.R. Potts, D. Zhan, L. Wang, C.K. Poh, C. Tang, H. Gong, Z. Shen, J. Lin, R.S. Ruoff, Energy Environ. Sci. 5 (2012) 7936.
- [80] C. Zhang, R. Hao, H. Liao, Y. Hou, Nano Energy 2 (2013) 88–97.
- [81] T. Xing, Y. Zheng, Li L, B.C.C. Cowie, D. Gunzelmann, S. Qiao, S. Huang, Y. Chen, ACS Nano 8 (2014) 6856–6862.
- [82] E. Brillas, I. Sires, M. Oturan, Chem. Rev. 109 (2009) 6570–6631.
- [83] Z. Qiang, J.-H. Chang, C.-P. Huang, Water Res. 37 (2003) 1308–1319.
- [84] X. Lou, C. Fang, Z. Geng, Y. Jin, D. Xiao, Z. Wang, J. Liu, Y. Guo, Chemosphere 173 (2017) 529–534.
- [85] K. Shang, X. Wang, J. Li, H. Wang, N. Lu, N. Jiang, Y. Wu, Chem. Eng. J. 311 (2017) 378–384.